JACS
JOURNAL OF THE AMERICAN CHEMICAL SOCIETY
Article
pubs.acs.org/JACS

Mechanoelectrochemical Catalysis of the Effect of Elastic Strain on a Platinum Nanofilm for the ORR Exerted by a Shape Memory Alloy Substrate

Minshu Du,[†,‡] Lishan Cui,[†] Yi Cao,[§] and Allen J. Bard*[,‡]

[†]State Key laboratory of Heavy Oil Processing and Department of Materials Science and Engineering, China University of Petroleum, Beijing 102249, China

[‡]Center for Electrochemistry, Department of Chemistry, The University of Texas at Austin, Austin, Texas 78712, United States

[§]Department of Materials Physics and Chemistry, University of Science and Technology Beijing, Beijing 100083, China

Supporting Information

ABSTRACT: Both the ligand effect and surface strain can affect the electrocatalytic reactivity. In that matter exists a need to be fundamentally understood; however, there is no effective strategy to isolate the strain effect in electrocatalytic systems. In this research we show how the elastic strain in a platinum nanofilm varies the catalytic activity for the oxygen reduction reaction, a key barrier to the wide applications of fuel cells. NiTi shape memory alloy was selected as the substrate to strain engineer the deposited Pt nanofilm in both compressively and tensilely strained states by taking advantage of the two-way shape memory effect for the first time. We demonstrate that compressive strain weakens the Pt surface adsorption and hence improves the ORR activity, which reflects in a 52% enhancement of the kinetic rate constant and a 27 mV positive shift of the half-wave potential for the compressively strained 5 nm Pt compared to the pristine Pt. Tensile strain has the opposite effect, which is in general agreement with the proposed d-band theory.

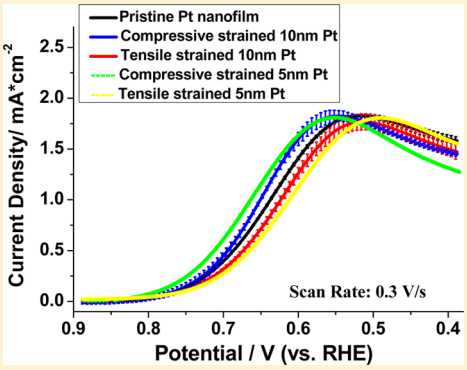

INTRODUCTION

Mechanoelectrochemistry involves the effect of mechanical energy on the thermodynamics and kinetics of electrochemical processes.[1] These include effects of strain and triboelectric processes. Recently, there has been interest in the effect of elastic strain on electrocatalytic processes in bimetallic core−shell structures.[2] The good correlation between the kinetics of the hydrogen evolution reaction and the bulk modulus of a metal is also suggestive of strain effects.[3] For example, in attempts to improve the electrocatalytic activity of Pt for the oxygen reduction reaction (ORR), Pt has been alloyed with other transition metals (e.g., Fe, Co, Cu, Ni, Ti) to form bimetallic catalysts with various surface structures.[4−8] Monolayer-on-metal and core−shell bimetallic structures are also obtained by deposition method and dealloying process.[9−12] In such core−shell structures, e.g., AuCu@Pt, the Pt shell is strained by the epitaxial growth on the mismatched AuCu lattice.[13] However, the effect of strain on the Pt layer is clouded by electronic effects in the interaction between the two metals (the ligand effect) and perhaps surface effects if any core atoms are exposed. These effects in general are simultaneously present and modulate the catalytic activity of bimetallic catalysts.[7]

So far, there have been no reports that allow one to isolate the strain effects in electrocatalytic systems. Here we have used a NiTi shape memory alloy (SMA) substrate to apply stress to a Pt nanofilm as an electrode for the ORR. An SMA undergoes reversible phase changes as a function of temperature, which is transmitted as stress to the surface nanofilm. The NiTi SMA substrate was mechanically predeformed to develop its two-way shape memory effect,[14] which enables "strain engineering" of the Pt nanofilm. Moreover, the NiTi SMA permits three elastic states of the Pt nanofilm to be obtained: unstrained, tensilely strained, and compressively strained as a function of temperature. In other words, the Pt nanofilm deposited on the NiTi substrate (unstrained) can be compressed by raising the temperature and then expanded by lowering the temperature, all with the same film in the same electrochemical cell. This approach thus appears more direct in finding mechanochemical effects than the core−shell nanoparticle structures where complicating effects, such as uncertainty of surface structure and area, dependence on preparation methods, particle size, and distribution in addition to the electronic structure effects, may be present. Thus, elastic strain effect as the main effect for the changes of Pt ORR activity was investigated in this paper, which provides a fundamental understanding and design strategy for the development of higher activity Pt-based electrocatalysts.

Received: March 23, 2015
Published: May 18, 2015

DOI: 10.1021/jacs.5b03034
J. Am. Chem. Soc. 2015, 137, 7397−7403

EXPERIMENTAL SECTION

SMA Preparation. The NiTi shape memory alloy ingot with a composition of Ti-50.0 at. % Ni was prepared by means of vacuum induction melting and then forged to be a ribbon with the thickness of 20 mm. The ribbon was further manufactured to be a sheet with the thickness of 1 mm by hot rolling.

After annealing at 600 °C for 20 min, the NiTi sheet was tensile deformed to 13% and then unloaded at room temperature using a WDW-200 material test system.[15] The specimens of 10 × 10 × 1 mm in size were cut from a predeformed NiTi sheet using a wire-cut electrical discharge machine. Differential scanning calorimetry (DSC) and thermal dilatation measurement were carried out to characterize the phase transformation behavior of the NiTi SMA after the deformation.

Pt Nanofilm Deposition. The polycrystalline 10 nm and 5 nm Pt nanofilms were deposited at room temperature on the predeformed NiTi substrate by direct current magnetron sputtering with a base pressure of 3.4×10^{-7} Torr and Ar working pressure of 4.2×10^{-3} Torr. A voltage of 350 V and a current of 50 mA were applied for deposition. The deposition rate was 0.055 nm/s, which was obtained by the measurement of the film thickness on the NiTi substrate after 30 min deposition using a stepper surface profilometry.

Crystal Structure Determination. Grazing incident X-ray diffraction (GIXRD) with Cu Kα radiation was employed on the R-Axis spider system (Rigaku Corporation) to analyze the crystal structure of Pt/NiTi sample. The technique parameters are set as ω = 190°, φ = 0°, χ = 55°. Search-Match software was used for peak identification and analysis.

Electrochemical Measurements. A glass rectangular cell of size 2 × 2 × 6 cm was used, which has a 1 cm diameter aperture containing an O-ring on one side; the inside diameter of the O-ring is ~7.5 mm. A Pt/NiTi working electrode was placed on top of the O-ring and was tightened under a Teflon plate using two connecting screws. Thus, the sample was exposed to the electrolyte, 0.5 M H_2SO_4 (Fisher, Fair Lawn, NJ) in the cell. All electrochemical measurements were conducted on an electrochemical workstation (CHI660D, CH Instrument). A standard three-electrode system was used employing Pt/NiTi disk working electrode, a Pt wire counter electrode, and an Ag/AgCl (0.1 M) reference electrode. A schematic diagram of the electrochemical cell is shown in Figure S1. All the potentials given in this paper have been converted to the reversible hydrogen electrode (RHE) scale at 25 °C.

For a complete cleaning, the Pt/NiTi disk electrode was immersed into a solution of hydrogen peroxide (10% v/v) + diluted sulfuric acid for 12 h and then rinsed gently with deionized water before each electrochemical experiment. First, a pristine unstrained Pt/NiTi sample was electrochemically activated in the Ar-saturated 0.5 M H_2SO_4 solution (1 atm) by cycling the potential between 1.5 and 0 V at a scan rate of 0.1 V/s for 50 cycles until reproducible voltammograms were obtained. These cycling potential limits were selected not to involve extensive oxygen and hydrogen evolution and thus not cause appreciable roughening of the Pt film surface. Then, the background current was measured in the Ar-saturated 0.5 M H_2SO_4 solution by linear sweep voltammetry (LSV) in the potential range of 0.9 to 0.4 V at a scan rate of 0.1 V/s. Then the ORR activity of unstrained Pt was measured by LSV in the potential range from 0.9 to 0.4 V in O_2-saturated 0.5 M H_2SO_4 (1 atm) at room temperature at a scan rate of 0.1 V/s. For better reproducibility, the activation process was repeated again in the Ar-saturated 0.5 M H_2SO_4 solution, and the background current and ORR activity of unstrained Pt were measured using a second scan rate of 0.3 V/s. Then, the same procedures were employed to measure the background current and ORR activity at the other three different scan rates of 0.5, 0.8, and 1.0 V/s. Second, the unstrained Pt/NiTi sample was heated to 200 °C and returned to room temperature under vacuum. During this thermal cycling process, the NiTi substrate contracted due to phase transformation, which caused compressive strain in the Pt nanofilm. The same chemical cleaning treatment and electrochemical activation processes were employed before the measurements of background current and the ORR activity on the compressively strained Pt at room temperature. Third, the unstrained Pt/NiTi sample was cooled from room temperature to lower temperature (≤ −100 °C, using a mixture of liquid nitrogen and ethanol) and returned to room temperature. During this thermal cycling process, the NiTi substrate expanded due to the phase transformation, which caused tensile strain in the Pt nanofilm. The same chemical cleaning treatment, electrochemical activation processes, and the measurements of both background current and ORR activity as mentioned before were performed on this tensilely strained Pt at room temperature.

Electrochemical Simulation. To compare the kinetic effects of compressive and tensile strain, it is useful to have a model of the electron-transfer reaction. The ORR is complex, and no clear analytical model exists. We chose to represent this by a simple n = 1 electron transfer with a Butler−Volmer formalism. Digital simulations were performed to obtain the kinetic parameters of ORR using DigiElch electrochemical simulation software (Gamry Instrument, 6.F version).

The simulation was carried out assuming 1D semi-infinite diffusion and a planar electrode geometry. The kinetic parameters of the ORR were obtained by finding the best-fit between experimental and simulated voltammograms. Among all the kinetic parameters, only the electron-transfer rate constant k was allowed to change through the fitting processes of different strained Pt nanofilms, while the formal potential E^0 and electron-transfer coefficient, α, maintain the same. The electrochemically active surface area (EASA) of the sample was calculated by integrating the charge of the hydrogen under potential desorption peaks after a double layer correction.

RESULTS AND DISCUSSION

Obtaining Different Elastic Strain States. NiTi is a typical shape memory material, and both one-way and two-way shape memory effects can be obtained after different thermomechanical treatments.[15] NiTi sheet was tensile deformed in the martensitic state to the strain of 13% at room temperature, during this process the martensite reoriented and further plastic deformed. After this predeformation, two-way shape memory effect existed in the NiTi substrate. DSC result (in Figure 1a) shows the first and second reverse martensitic transformation (martensite → parent) started from 73 and 26 °C, respectively, and martensitic transformation (parent → martensite) started from 35 °C. This reversible phase transformation accompanied by a tremendous change of sample length, as shown in Figure 1b, NiTi contracted 7.5% in the first reverse martensitic transformation during heating and then expanded 4% during the cooling process from 200 °C to −100 °C due to martensitic transformation; this 4% strain could recover again in the following heating process. Therefore, NiTi exhibited a reversible two-way memory strain of ε = 4%. It is noticed that the transformation measured by thermal dilatation appeared to exhibit a hysteretic delay as compared to the DSC measurement, e.g., lower values for T_M and higher values for T_A. This is mainly attributed to the difference in the heating/cooling method of the two techniques as well as the features of the thermal and dimensional measurements adopted by these two techniques.[15]

By taking advantage of the two-way shape memory effect of NiTi SMA, a Pt nanofilm deposited on this substrate can be placed into a state with a large amount of elastic strain. From Figure 1b, the room temperature deposited Pt/NiTi sample represented as "(1)" is unstrained (the lattice mismatch of Pt and NiTi is negligible), and we call this Pt as being in a "pristine state". The pristine Pt nanofilm was electrochemically activated in the Ar-saturated 0.5 M H_2SO4 solution, and its ORR activity was then tested by LSV in the O_2-saturated 0.5 M H_2SO4 at 5

DOI: 10.1021/jacs.5b03034
J. Am. Chem. Soc. 2015, 137, 7397−7403

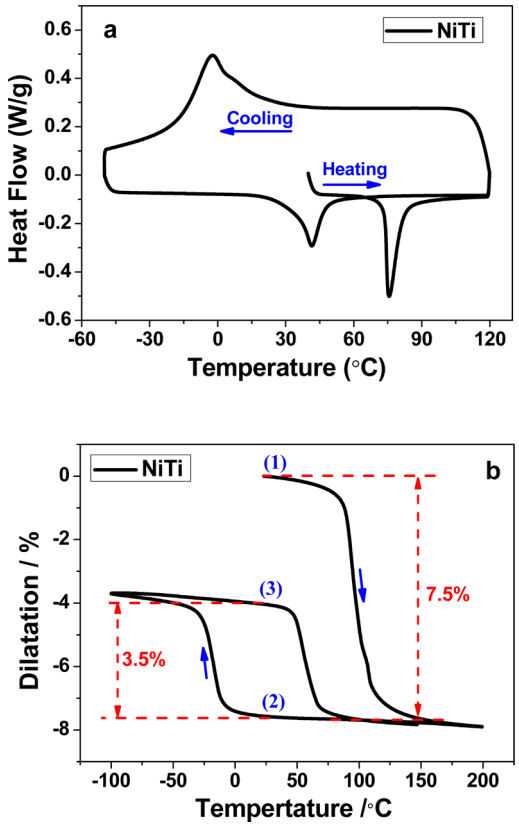

Figure 1. Phase transformation behavior of predeformed NiTi substrate: (a) DSC measurement; (b) thermal dilatation measurement, in which (1) indicates a pristine state of Pt and (2) and (3) indicate a compressively strained state and tensilely strained state of Pt.

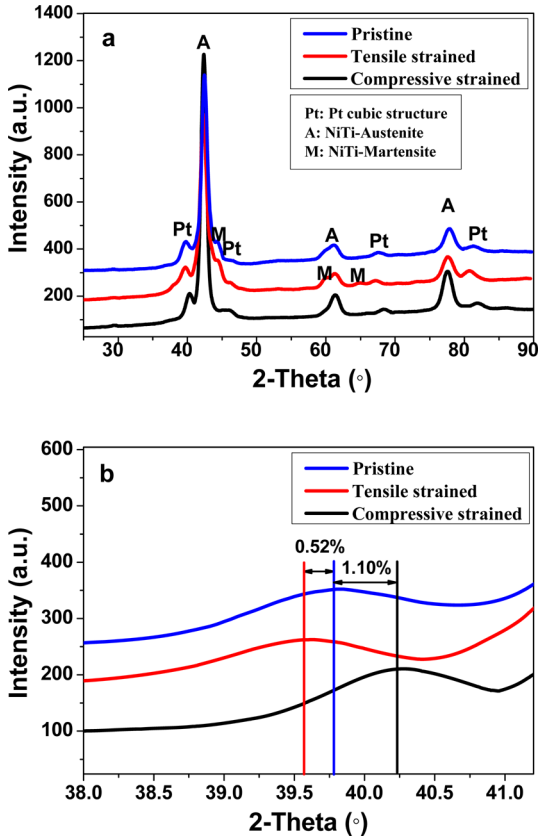

Figure 2. GIXRD pattern of a 10 nm Pt/NiTi substrate sample: (a) whole XRD pattern; (b) enlargement of Pt-(111) diffraction peak.

different scan rates at room temperature. Next, the sample was heated to 200 °C and returned to room temperature under vacuum to produce state "(2)". During the heating process, the NiTi substrate contracted due to a reverse martensitic transformation, which also caused a contraction of the Pt nanofilm. This contraction remained essentially the same when cooled from 200 °C to room temperature. As a result, the Pt nanofilm was under 7.5% compressive strain in the "(2)" state, assuming interfacial bonding between the Pt and NiTi substrate is strong and the intrinsic elastic strain limit of polycrystalline Pt is large, so that this Pt is under a "compressively strained state". Similarly, the NiTi substrate was heated to 200 °C followed by returning to room temperature, and then a Pt nanofilm was deposited onto it. Then further cooled from room temperature to a temperature ≤ -100 °C (using a mixture of liquid nitrogen and ethanol) and returned to room temperature to produce state "(3)". The Pt under a "tensilely strained state" of up to 3.5% is attained, again assuming strong bonding between Pt and NiTi and the 3.5% strain not exceeding the intrinsic strain limit of the Pt nanofilm. In short, three different strained states—pristine state, compressively strained state and tensilely strained state of Pt nanofilm can be obtained respectively by the different thermal cycling treatments.

Crystal structures of the 10 nm Pt/NiTi samples under different strain states were characterized by grazing-incident X-ray diffraction. As shown in Figure 2a, both the diffraction peaks from NiTi substrate and the 10 nm Pt nanofilm are detected. Three strong peaks belong to the NiTi B2 parent phase, three weak peaks belong to the monoclinic NiTi martensite, and four peaks belong to the cubic structural Pt with a space group of $Fm\bar{3}m$. Note that the peak intensity of the Pt (111) plane with a 2-θ angle of about 40° is about 7 times as high as that of the Pt (200) and (220) plane, however for standard nontextured polycrystalline Pt, the (111) peak intensity is just 2−3 times as high as that of the other two peaks. So it is clear that the prepared Pt nanofilm has a strongly preferred crystallographic orientation in the (111) direction, and the position shifts of this (111) peak under different strain states are clear. Gaussian fits were used to determine the peak positions. As shown in Figure 2b, the (111) peak position of tensilely strained Pt shifts toward low angles compared to the peak position of the pristine Pt; this implies a larger d-spacing value of the tensilely strained Pt lattice. Moreover, the (111) peak position of compressively strained Pt shifts toward high angles compared to the peak position of the pristine Pt; this implies a smaller d-spacing in the compressively strained Pt lattice. Bragg's law was used to calculate the d-spacing value, where d_0, d_1, and d_2 represent the (111) d-spacing of the pristine Pt, compressively strained Pt, and tensilely strained Pt, respectively. Note that only elastic strain, not plastic strain, can change the lattice parameters or a crystal structure with a subsequent change in the electronic properties of a material. The elastic strain value was calculated by eq 1:

$$\text{elastic strain}(\%) = \left(\frac{d_{1\text{or}2} - d_0}{d_0}\right) \times 100\% \quad (1)$$

Thus, 7.5% contraction of NiTi substrate leads to only 1.10% compressive strain of 10 nm Pt upon it, and 3.5% expansion of NiTi substrate leads to 0.52% tensile strain of 10 nm Pt. Three

DOI: 10.1021/jacs.5b03034
J. Am. Chem. Soc. 2015, 137, 7397−7403

speculations account for this phenomenon: First, stress-induced martensite generating near the interface might release partial stress (strain), because there is a large interaction stress existing in the interface when the NiTi substrate contracts or expands during the thermal cycling process. Stress-induced martensite may generate at the interface between the Pt nanofilm and NiTi substrate if the interfacial stress exceeds the critical stress for stress-induced martensite transformation. Second, load transfer between substrate and nanofilm is low due to slightly weak interfacial bonding compared to that of epitaxial structure. Third, the intrinsic elastic strain limit of a polycrystalline 10 nm Pt nanofilm is unknown and may be much smaller than 7.5%. The only reported stress−strain plot for a 400 nm Pt nanofilm shows that the elastic strain limit is only 1.5%.[16] As a result, 7.5% contraction of the NiTi substrate probably induced quite a small elastic strain (~1.10%) of Pt at the beginning and then followed by a large plastic deformation of the Pt. It should be noted that the magnitude of strain obtained from the GIXRD result is the average strain for the whole 10 nm thick Pt film, and it is difficult to evaluate the magnitude of the strain at the film surface. In conclusion, both the compressive strain and tensile strain can be successfully exerted to a 10 nm Pt nanofilm by taking advantage of the two-way shape memory effect of NiTi substrate, but the elastic strain at the surface of the Pt film is probably small and not as large as we designed and expected.

ORR of Pristine Pt Nanofilm. Calculations suggest that even small elastic strain can cause the apparent change of electrocatalytic activity of Pt.[17−19] Here, ORR activities of the Pt nanofilm under different strain states were investigated by linear sweep voltammetry in the O_2-saturated (1 atm) aqueous solutions of 0.5 M H_2SO_4. Before each experiment, as described earlier in the Experimental Section, the Pt/NiTi electrode was electrochemically activated in the Ar-saturated 0.5 M H_2SO_4 solution (1 atm) by cycling the potential between 1.5 and 0 V at a scan rate of 0.1 V/s for 50 cycles until reproducible voltammograms were obtained.[20,21] The hydrogen under potential desorption peaks was used to calculate the electrochemically active surface area (EASA), which was estimated by

$$\text{EASA} = \frac{Q}{\text{scan rate} \times 2.1 \times 10^{-4}} \quad (2)$$

Here, Q is obtained by integrating the charge passed during the hydrogen desorption from the electrode surface after double-layer correction, assuming that the charge required to oxidize a monolayer of hydrogen on polycrystalline Pt is 0.21 mC/cm^2.[22] The EASA of pristine state 10 nm Pt/NiTi sample was determined to be 0.381 cm^2. The nonfaradaic background current of Pt was measured at different scan rates in the potential range from 0.9 to 0.4 V vs RHE, the forward scan polarization curves are shown in Figure 3a. Then, its ORR activity was measured in the O_2-saturated (1 atm) 0.5 M H_2SO_4 solution at a scan rate of 0.1, 0.3, 0.5, 0.8, and 1.0 V/s. A series of polarization curves are shown in Figure 3b after subtracting background current. Note that our (111)-textured polycrystalline pristine state Pt nanofilm shows a relatively inferior ORR activity compared to that of previous reported nontextured polycrystalline Pt in sulfuric acid solution.[23,24] According to the literature,[25,26] (bi)sulfate ions that are known to inhibit the ORR in dilute sulfuric acid solution adsorb most strongly on Pt (111) planes in terms of the symmetry match between the fcc (111) facet and the trigonal coplanar geometry of the oxygen in the sulfate anions.

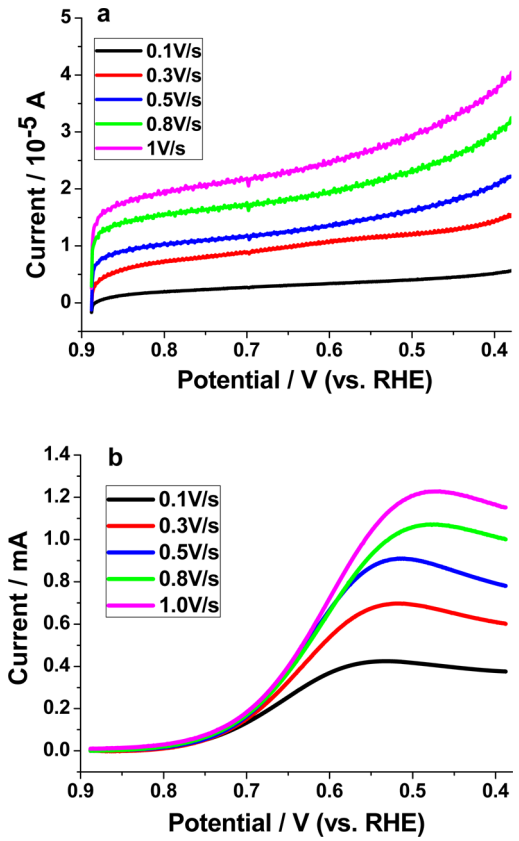

Figure 3. Polarization curves of the pristine state 10 nm Pt (deposited at room temperature) at different scan rates in the (a) Ar-saturated 0.5 M H_2SO_4 solution and (b) O_2-saturated 0.5 M H_2SO_4 solution at room temperature.

Digital simulations were performed to obtain the kinetic parameters of ORR using DigiElch electrochemical simulation software. The mechanism of the ORR reaction on Pt is complicated and involves transfer of four electrons, four protons, and an oxygen-bond cleavage. The mechanism of ORR on Pt in the acid solution remains unclear, e.g., Yeager,[27] Damjanovic,[28] and Nørskov[29] have suggested different mechanisms. To simplify the simulation process here, we only considered a one-electron-transfer process in a Butler−Volmer process. Therefore, the current in Figure 3b is divided by 4 to compare the experimental results to those of the simulation that assumed a 1D semi-infinite diffusion mass transfer with EASA of pristine Pt/NiTi disk electrode of 0.381 cm^2, the diffusion coefficient of oxygen as 2×10^{-5} cm^2/s.[30] The concentration of oxygen was about 0.95 mM. Kinetic parameters of ORR including formal potential E^0, electron-transfer coefficient α, and rate constant k can be acquired by simulating a series of $i-V$ curves with five different scan rates, and the best fit results are shown in Figure 4. While the values of the obtained parameters have little meaning in terms of the more complicated mechanism, they are useful in intercomparing the results of the effect of strain, assuming the strain does not change the mechanism of the ORR.

ORR of Compressively and Tensilely Strained Pt Nanofilm. In studying the ORR on the strained Pt nanofilms, the same procedures as employed with the pristine Pt sample were applied. Thus, for each, the background current in the Ar-saturated solution and the ORR activity in the O_2-saturated 0.5 M H_2SO_4 solution were measured as shown in Figures S2 and

DOI: 10.1021/jacs.5b03034
J. Am. Chem. Soc. 2015, 137, 7397−7403

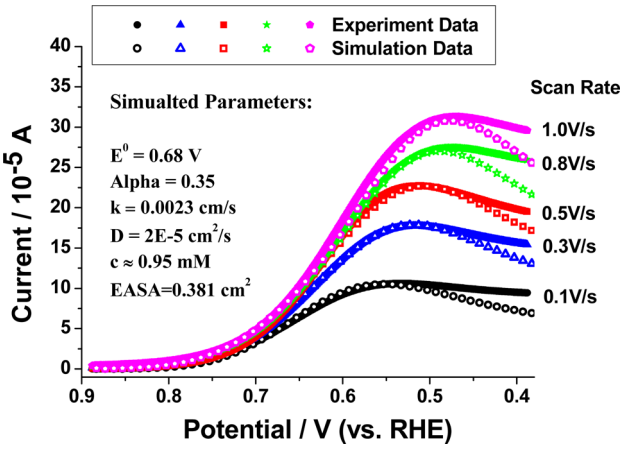

Figure 4. Experimental and simulated results of ORR of pristine state 10 nm Pt in the O_2-saturated 0.5 M H_2SO_4 solution.

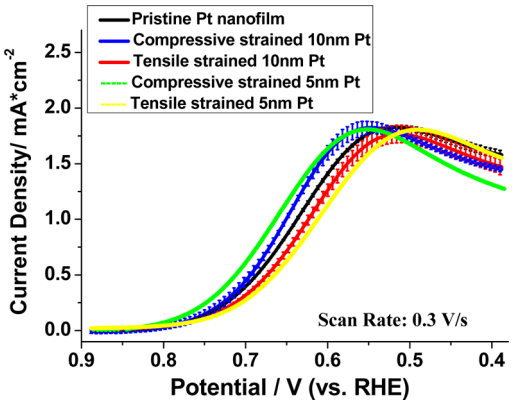

Figure 5. Polarization curves of the ORR of 10 and 5 nm Pt nanofilm under different strain states at a scan rate of 0.3 V/s. The data of 10 nm Pt nanofilm are shown with standard deviation.

S4. Simulated results of the ORR of compressively and tensilely strained Pt are shown in Figures S3 and S5, respectively.

In addition, two more repeated experiments were conducted on two other pristine 10 nm Pt samples, compressively strained and tensilely strained 10 nm Pt samples. Thus, three independent measurements on each form were made. From simulated results shown in Figures S6–S8, the reliability of this experiment is quite good. All of the kinetic parameters of 10 nm Pt nanofilm under different strain states are listed in Table 1.

Dependence of the Strain Effects on Thickness of Pt Nanofilm. Because the elastic strain is transferred from the NiTi substrate to the Pt nanofilm, an interfacial Pt layer should have the largest elastic strain and the strain in each layer of Pt decreases progressively with an increase of film thickness. Thus, larger elastic strain and stronger strain effects at the Pt surface should be present in thinner Pt nanofilm. The same experiments were also carried out with a 5 nm Pt nanofilm deposited on the same predeformed NiTi SMA substrate. The same chemical cleaning and electrochemical activation procedures were used before the measurement of the ORR. The pristine, compressively strained, and tensilely strained states of 5 nm Pt were obtained by the different thermal cycling processes as employed with the 10 nm Pt. Thus, for each, the background current in the Ar-saturated solution and the ORR activity in the O_2-saturated 0.5 M H_2SO_4 solution were measured. The experimental and simulated results are presented in Figures S9–S14.

Strain Effect on the ORR Activity and Its Mechanism. The comparison of ORR polarization curves of the Pt nanofilm under different strain states at a scan rate of 0.3 V/s is shown in Figure 5, and the data for 10 nm Pt shown with standard deviation. The kinetic rate constants and half-wave potentials of the ORR of the Pt nanofilm under different strain rates are compared in Figure 6. It is concluded that the compressively strained Pt nanofilm exhibits higher ORR activity than that of

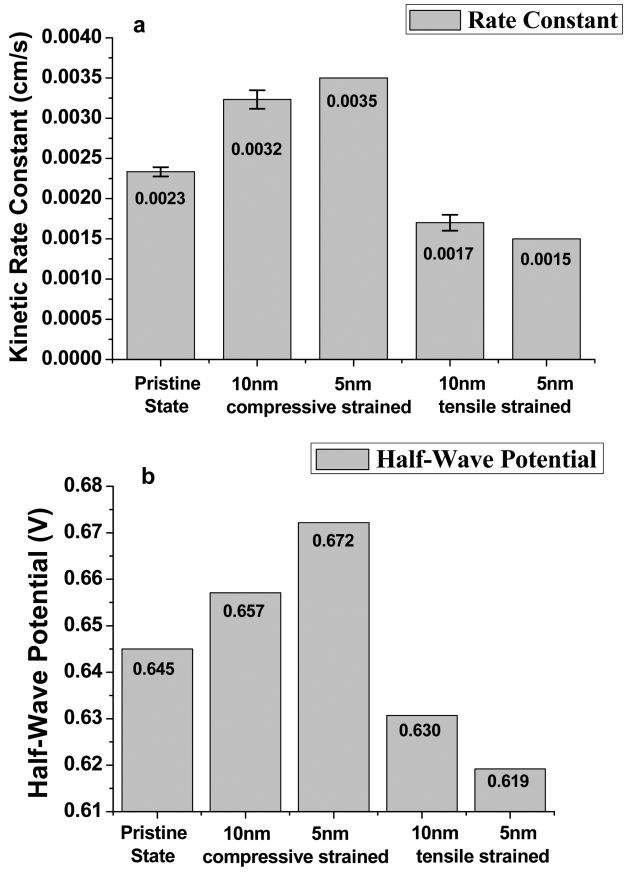

Figure 6. Comparison of the ORR activity of 10 and 5 nm Pt nanofilm under different strain states at a scan rate of 0.3 V/s: (a) Kinetic rate constants. Bars show ± σ (standard deviation of three measurements). (b) Half-wave potentials.

Table 1. Kinetic Parameters of the ORR of 10 nm Pt under Different Strain States Obtained by Simulation

kinetic parameters	pristine 10 nm Pt	compressive strained 10 nm Pt	tensile strained 10 nm Pt
E^0 (V vs RHE)	0.68	0.68	0.68
α	0.35	0.35	0.35
k (cm/s)	0.0023 ± 8.2 × 10^{-5}	0.0032 ± 2.2 × 10^{-4}	0.0017 ± 1.4 × 10^{-4}

*The other simulated parameters include: oxygen diffusion coefficient is 2 × 10^{-5} cm^2/s, oxygen concentration, and EASA for each state of Pt/NiTi sample are shown in Figures 4, S3, and S5–S8.

DOI: 10.1021/jacs.5b03034
J. Am. Chem. Soc. 2015, 137, 7397–7403

the pristine Pt, and the tensilely strained Pt nanofilm exhibits the lowest activity. The strain effects on the ORR activity of 5 nm Pt are relatively larger than those of 10 nm Pt due to larger elastic strain exerted in the thinner Pt nanofilm. Approximately, the compressive strain of 5 nm Pt is 1.93%, and the tensile strain of 5 nm Pt is 0.76%, shown in Figure S15.

The Pt/NiTi samples under different strain states of Pt are all composed of the polycrystalline Pt nanofilm and NiTi substrate of the same chemical composition, thus, the ligand effects, if they exist, would be almost eliminated when considering the strain effects on the ORR activity. To gain insight into how the elastic strain of Pt nanofilm affects the ORR activity, careful inspection of the activation voltammograms was conducted. Taking 10 nm Pt, for example, shown in Figure 7, revealed an

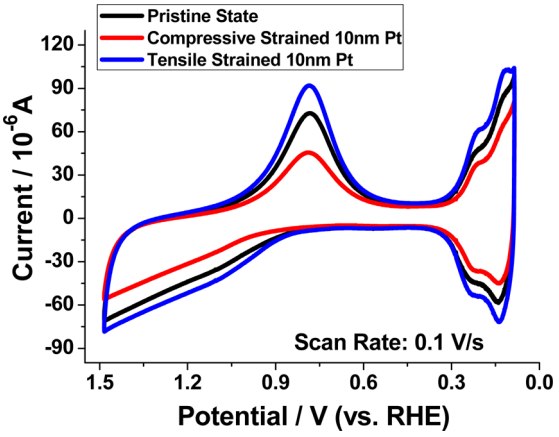

Figure 7. Cyclic voltammograms of the 10 nm Pt nanofilm under different strain states in the Ar-saturated 0.5 M H_2SO_4 solution at a scan rate of 0.1 V/s.

obvious distinction of the potential-dependent surface adsorption of hydrogen ($H^+ + e^- = H_{upd}$) between 0.05 V < E < 0.4 V and hydroxyl species ($2H_2O = OH_{ad} + H_3O^+ + e^-$) above 0.8 V. There is a negative shift in H_{upd} formation and a positive shift in OH_{ad} formation that occurred in the compressively strained Pt nanofilm relative to the pristine Pt. In agreement with the shifts of the onset potential of adsorption, the fractional coverages by H_{upd} and OH_{ad} of the compressively strained 10 nm Pt were significantly reduced relative to those of the pristine Pt nanofilm. Considering the geometric areas of the Pt/NiTi samples are the same (the geometric area of the working electrode is defined by the inside diameter of the O-ring on the electrochemical cell), both phenomena implied a weaker adsorption of adsorbates on the compressively strained Pt surface. Meanwhile, the tensilely strained 10 nm Pt shows the opposite effects. The d-band model developed by Nørskov and co-workers has successfully related the adsorption properties of rate-limiting intermediates to the electronic structure of the catalyst.[9,31,32] For simple adsorbates such as the ORR intermediates O and OH, a simple electron-interaction model was investigated, in which the adsorbate valence p-level forms bonding and antibonding states with the Pt d-band.[31,33] Building on this theory, it could be speculated that the compressive strain in the Pt lattice leads to the increasing overlap of the Pt d-band, which results in a downshifting of the d-band center. The downshift pulls antibonding states further below the Fermi level and increases Pauli repulsion. As a result, compressive strain weakens the Pt surface bonding with adsorbates and induces higher ORR activity, while tensile strain has the opposite effect.

CONCLUSION

In this study, the NiTi shape memory alloy (SMA) was chosen as the substrate to strain engineer the deposited 5 and 10 nm thick Pt nanofilms in order to vary the strain and enhance the ORR activity. The strain variation mechanism of the Pt nanofilm originates from the two-way shape memory effect of the NiTi substrate. After two different thermomechanical treatments, confirmed by GIXRD analysis, compressive and tensile strains were successfully applied to the Pt nanofilm. The elastic strain effect instead of the ligand effect plays a role in the electrocatalytic performance of the Pt nanofilm for the ORR. The compressive strain of the Pt nanofilm improves the ORR activity, which reflects in a 52% enhancement of the kinetic rate constant and a 27 mV positive shift of the half-wave potential for the compressively strained 5 nm Pt compared to the pristine Pt. Conversely, the tensile strain leads to a 35% decrease of the rate constant and a 26 mV negative shift of the half-wave potential for the 5 nm Pt. This is in general agreement with the proposed d-band theory, where it is speculated that the d-band center of the Pt nanofilm shifts because of different strain states with a change in surface adsorption and finally a variation of the catalytic reactivity. This report offers direct evidence that both tensile and compressive strain in a Pt nanofilm can be exerted by the NiTi SMA substrate, although it is difficult to evaluate the magnitude of the strain at the film surface based on substrate strain and film thickness. In addition, control of the elastic strain value by the preloading magnitude of the SMA and the thickness of the nanofilm is a promising one.

ASSOCIATED CONTENT

Supporting Information

Schematic diagram of three electrodes electrochemical cell, LSV curves of the ORR of the compressively strained 10 nm Pt and tensilely strained 10 nm Pt, LSV curves of the ORR of the pristine, compressively strained and tensilely strained 5 nm Pt nanofilm, and the corresponding DigiElch simulation results of them, and the GIXRD pattern of the 5 nm Pt-NiTi substrate sample. The Supporting Information is available free of charge on the ACS Publications website at DOI: 10.1021/jacs.5b03034.

AUTHOR INFORMATION

Corresponding Author

*ajbard@mail.utexas.edu

Notes

The authors declare no competing financial interest.

ACKNOWLEDGMENTS

This work was supported by the NSF CCI Solar Fuels grant (CHE-1305124). The Welch Foundation (F-0021) supported A.J.B. The Key National Natural Science Foundation of China (NSFC) (51231008) founded the preparation and predeforming of the NiTi substrate and the deposition of the Pt nanofilm. M.D. is grateful for the support of the China Scholarship Council (CSC) and Microstructure Laboratory For Energy Materials of China University of Petroleum, Beijing. M.D. thanks Dr. Yao Meng, Dr. Fahe Cao, and Dr. Netzahualcóyotl Arroyo-Currás for help with the electrochemical experiment,

DOI: 10.1021/jacs.5b03034
J. Am. Chem. Soc. 2015, 137, 7397−7403

Brent Bennett for discussion of the DigiElch simulation, and Dr. Vincent Lynch for the help with the GIXRD measurement.

REFERENCES

(1) Jones, W.; Eddleston, M. D. *Faraday Discuss.* **2014**, *170*, 9−34.
(2) Sasaki, K.; Naohara, H.; Cai, Y.; Choi, Y. M.; Liu, P.; Vukmirovic, M. B.; Wang, J. X.; Adzic, R. R. *Angew. Chem., Int. Ed.* **2010**, *49*, 8602−8607.
(3) Leonard, K. C.; Bard, A. J. *J. Am. Chem. Soc.* **2013**, *135*, 15885−15889.
(4) Stamenkovic, V.; Mun, B. S.; Mayrhofer, K. J.; Ross, P. N.; Markovic, N. M.; Rossmeisl, J.; Greeley, J.; Nørskov, J. K. *Angew. Chem., Int. Ed.* **2006**, *118*, 2963−2967.
(5) Stamenkovic, V. R.; Fowler, B.; Mun, B. S.; Wang, G. F.; Ross, P. N.; Lucas, C. A.; Markovic, N. M. *Science* **2007**, *315*, 493−497.
(6) Stephens, I. E. L.; Bondarenko, A. S.; Perez-Alonso, F. J.; Calle-Vallejo, F.; Bech, L.; Johansson, T. P.; Jepsen, A. K.; Frydendal, R.; Knudsen, B. P.; Rossmeisl, J.; Chorkendorff, I. *J. Am. Chem. Soc.* **2011**, *133*, 5485−5491.
(7) Strasser, P.; Koh, S.; Anniyev, T.; Greeley, J.; More, K.; Yu, C. F.; Liu, Z. C.; Kaya, S.; Nordlund, D.; Ogasawara, H.; Toney, M. F.; Nilsson, A. *Nat. Chem.* **2010**, *2*, 454−460.
(8) Stephens, I. E. L.; Bondarenko, A. S.; Gronbjerg, U.; Rossmeisl, J.; Chorkendorff, I. *Energy Environ. Sci.* **2012**, *5*, 6744−6762.
(9) Zhang, J. L.; Vukmirovic, M. B.; Xu, Y.; Mavrikakis, M.; Adzic, R. R. *Angew. Chem., Int. Ed.* **2005**, *44*, 2132−2135.
(10) Zhang, S.; Zhang, X.; Jiang, G. M.; Zhu, H. Y.; Guo, S. J.; Su, D.; Lu, G.; Sun, S. H. *J. Am. Chem. Soc.* **2014**, *136*, 7734−7739.
(11) Wu, J. B.; Li, P. P.; Pan, Y. T.; Warren, S.; Yin, X.; Yang, H. *Chem. Soc. Rev.* **2012**, *41*, 8066−8074.
(12) Zhang, L.; Iyyamperumal, R.; Yancey, D. F.; Crooks, R. M.; Henkelman, G. *ACS Nano* **2013**, *7*, 9168−9172.
(13) Yang, J. H.; Chen, X. J.; Yang, X. F.; Ying, J. Y. *Energy Environ. Sci.* **2012**, *5*, 8976−8981.
(14) Otsuka, K.; Wayman, C. M. *Shape Memory Materials*; Cambridge University Press: Cambridge, U.K., 1999; p 36.
(15) Liu, Y. N.; Liu, Y.; Van Humbeeck, J. *Acta Metall.* **1998**, *47*, 199−209.
(16) Jonnalagadda, K.; Chasiotis, I.; Yagnamurthy, S.; Lambros, J.; Pulskamp, J.; Polcawich, R.; Dubey, M. *Exp. Mech.* **2010**, *50*, 25−35.
(17) Mavrikakis, M.; Hammer, B.; Norskov, J. K. *Phys. Rev. Lett.* **1998**, *81*, 2819−2822.
(18) Kattel, S.; Wang, G. F. *J. Chem. Phys.* **2014**, *141*, 124713.
(19) Sarkar, S.; Aquino, W. *Electrochim. Acta* **2013**, *111*, 814−822.
(20) Hoare, J. P. *Electrochim. Acta* **1982**, *27*, 1751−1761.
(21) Fernandez, J. L.; Bard, A. J. *Anal. Chem.* **2003**, *75*, 2967−2974.
(22) Pozio, A.; De Francesco, M.; Cemmi, A.; Cardellini, F.; Giorgi, L. *J. Power Sources* **2002**, *105*, 13−19.
(23) Paulus, U. A.; Schmidt, T. J.; Gasteiger, H. A.; Behm, R. J. *J. Electroanal. Chem.* **2001**, *495*, 134−145.
(24) Hsueh, K. L.; Gonzalez, E. R.; Srinivasan, S. *Electrochim. Acta* **1983**, *28*, 691−697.
(25) Markovic, N. M.; Lucas, C. A.; Gasteiger, H. A.; Ross, P. N. *Surf. Sci.* **1996**, *365*, 229−240.
(26) Macia, M. D.; Campina, J. M.; Herrero, E.; Feliu, J. M. *J. Electroanal. Chem.* **2004**, *564*, 141−150.
(27) Huang, J. C.; Sen, R. K.; Yeager, E. *J. Electrochem. Soc.* **1979**, *126*, 786−792.
(28) Damjanov, A.; Brusic, V. *Electrochim. Acta* **1967**, *12*, 615−628.
(29) Rossmeisl, J.; Karlberg, G. S.; Jaramillo, T.; Norskov, J. K. *Faraday Discuss.* **2008**, *140*, 337−346.
(30) Jamnongwong, M.; Loubiere, K.; Dietrich, N.; Hebrard, G. *Chem. Eng. J.* **2010**, *165*, 758−768.
(31) Hammer, B.; Norskov, J. K. *Nature* **1995**, *376*, 238−240.
(32) Nilsson, A.; Pettersson, L. G. M.; Hammer, B.; Bligaard, T.; Christensen, C. H.; Norskov, J. K. *Catal. Lett.* **2005**, *100*, 111−114.
(33) Nilsson, A.; Pettersson, L. G.; Norskov, J. *Chemical bonding at surfaces and interfaces*; Elsevier: Oxford, U.K., 2011; p 75.

DOI: 10.1021/jacs.5b03034
J. Am. Chem. Soc. 2015, 137, 7397−7403